Int J Adv Manuf Technol (2016) 83:1847–1859
DOI 10.1007/s00170-015-7609-x

ORIGINAL ARTICLE

A finite element model of thermal evolution in laser micro sintering

Jie Yin[1] · Haihong Zhu[1] · Linda Ke[1] · Panpan Hu[1] · Chongwen He[1] · Hu Zhang[1] · Xiaoyan Zeng[1]

Received: 25 July 2014 / Accepted: 19 July 2015 / Published online: 21 August 2015

Abstract Laser micro sintering (LMS) is a promising technique for micro-additive manufacturing. During LMS of metallic powder, the material property variation and the heat input energy profile are important to understand physical phenomena involved. This paper presents a finite element temperature distribution profile in LMS of nickel powder on 304 stainless steel substrate. The simulation considered the transition of powder-to-dense sub-model which involves effective thermal conductivity, volumetric enthalpy, and absorptance change; and a moving volumetric Gaussian distribution heat source sub-model. It is found that, for a specified cross section, the mechanism of preheating the nickel powder changes for the heat source from previous laser-irradiated substrate region to molten nickel as the laser beam approaches, while the center of molten pool slice is slightly shifted toward the reverse direction of laser scanning when the laser moves away due to the thermal accumulation effect. Simulated sintered widths showed very good agreement with experimental measurement, and relative prediction errors are below 16 % within the process window.

Keywords Additive manufacturing · Laser micro sintering · Numerical simulation · Temperature distribution · Pre- and post- heating

✉ Haihong Zhu
Zhuhh@hust.edu.cn

[1] Wuhan National Laboratory for Optoelectronics, School of Optical and Electronic Information, Huazhong University of Science and Technology, Wuhan 430074, People's Republic of China

1 Introduction

Laser micro sintering (LMS) was started in 2001 at Laserinstitut of Hochschule Mittweida [1]. LMS can fabricate intricate micro three-dimensional parts directly from powder material. The resolution and surface roughness obtained by this new technology was more than one order of magnitude better than those fabricated by conventional selective laser sintering (SLS) process [2]. Therefore, LMS attracted more and more attention in these years [3, 4]. During the LMS process, a powder layer thin as tens of micrometers is laser-scanned to fuse the two-dimensional slice to an underlying solid piece, which consists of a series of stacked and fused two-dimensional slices. After laser scanning, a fresh powder layer is spread and the scanning process is repeated. LMS is characterized by multiple models of heat mass transfer and chemical reactions that make the process very complex. Numerical simulation of physical process can generate better understanding which may be difficult for the conventional experimentation procedure.

The final properties of sintered parts fabricated by LMS depend on the material properties and on the laser heat input profile. The material state of the sintered sample changes with the evolution of the temperature and the microstructure including the porosity irreversibly decreasing and the phase change. Therefore, numerical models need to consider not only the temperature-dependent material properties but also the transition from powder phase to dense phase during laser powder processing. The effect of the powder-to-dense transition has been taken into account in three-dimensional finite element models to investigate temperature distribution by previous the studies. Dai and Shaw [5] developed a finite element model to investigate the temperature distribution, transient and residual stresses by using the powder-

to-dense transition and the moving surface heat source. Kolossov et al. [6] established a finite element model to predict temperature evolution on the surface of titanium powder layer during SLS, considering nonlinear behavior of thermal conductivity and specific heat due to temperature change and phase transition. Based on the phase transition from the powder phase to the dense phase during additive layer manufacturing, Roberts et al. [7] demonstrated the thermal behavior during the laser melting of metal powders. Dong et al. [8] studied density evolution and temperature development during the SLS process of polycarbonate powder by establishing a transient three-dimensional finite element model with phase transition and bi-level structure integration procedure. Hussein et al. [9] and Sun et al. [10] further demonstrated the temperature distribution, molten pool dimension, and thermal stresses during the selective laser melting (SLM). However, in order to simplify the powder-to-dense transition modeling process, most previous researchers have assumed a constant value for the laser absorptance of the material. Moreover, the variation of powder absorptance during laser processing has been reported. Kizaki et al. [11] and Tolochko et al. [12] have studied the variation of metallic powder absorptance for CO_2 and Nd:YAG laser processing, respectively. Taylor [13] found that during the CO_2 laser processing of stainless steel 314S powder, the calorimetric absorptance varied from 0.13 at the first scan down to 0.054 at the fourth re-scanning. Thus, the absorptance change should be taken consideration into the LMS finite element model.

Furthermore, it is important to emphasize that numerical analysis of LMS for metallic powder process should not only be attributed to powder-to-dense phase transition sub-model but also should include a more realistic heat input profile to establish a more accurate set of process. The optical penetration depth of the radiation into the powder bed was measured and simulated by using a ray tracing model [14] which takes multiple reflection and absorption of light on random particles arrangement into consideration. The ray tracing model shows a good coincidence when comparing the results with the experimental data. The conduction heat transfer is not included. During the very first time domain of the laser energy input into the powder bed, for the microscopic view of individual metallic particles, the energy is absorbed in a very narrow depth according to the penetration depth into the dense metal. But for the macroscopic view of the whole powder bed, owing to the multiple reflection and absorption effect, the actual optical penetration depth is larger than that in dense materials (the optical penetration depth for nickel powders with median grain size of 50–70 μm is 200 μm, while it is less than 100 nm for dense metals [15]), indicating that the optical properties of metallic powders show clear discrepancy with respect to those of the dense material. Moreover, for the point of view of the finite element method, if the minimum elementary size is much larger than the optical penetration depth, the laser heat source can be considered as a surface distributed energy. These are the reasons that many literature reports treated laser beam energy as the surface heat source. However, in contrast to the modeling of the SLS processing, due to the tens of micrometers of the laser spot diameter as well as the sintering specimen during the modeling of the LMS processing, the element size should be even smaller and can be comparable to the optical penetration depth. The surface distributed energy coupling may not be appropriate for laser powder micro sintering processing. Therefore, the laser heat source should be considered as a volumetric heat source in the LMS finite element model.

In this paper, a three-dimensional finite element model has been developed, using the subroutine in ANSYS Parametric Design Language (APDL^{TM}) environment for single nickel powder layer with Fe-304 stainless steel substrate owing to laser irradiation for LMS. Moreover, this model encompasses the powder-to-dense transition sub-model involving effective thermal conductivity, volumetric enthalpy, and absorptance change in combination with a sub-model of moving laser beam with a volumetric Gaussian distribution. The temperature field distribution and the evolution of the molten pool were investigated for the pre-heating effect on rear non-irradiated region and the post-heating effect on fore laser-irradiated region. Furthermore, the simulated sintered widths obtained were compared with the experimental measurements and the differences between them were discussed.

2 Physical description of LMS

Owing to random and complex nature of LMS process, following assumptions are made in this work:

- The whole powder bed is considered to be homogeneous and continuous media.
- During the sintering process, the thermophysical properties of the powder bed such as effective thermal conductivity, volumetric enthalpy, and absorptance are varied with temperatures and phase transition.
- To simplify the calculation, the powder layer shrinkage is ignored.
- The thermal history of heat affected zone is made by the effects of conduction, convection, and radiation. In addition, the combined heat transfer coefficient is used for the general effect of radiation and convection on the surface of the powder bed.
- The input volumetric heat flux due to laser irradiation is treated as an internal heat generation in the powder layer.

In modeling the heat transfer problem during LMS process, the first law of thermodynamics states that thermal energy is conserved and can be mathematically described as:

$$\rho C \frac{\partial T}{\partial t} = k\left(\frac{\partial^2 T}{\partial x^2} + \frac{\partial^2 T}{\partial y^2} + \frac{\partial^2 T}{\partial z^2}\right) + \dot{q} \tag{1}$$

where ρ represents the material density, C is the specific heat capacity, t is the interaction time between laser and the powder bed, k denotes thermal conductivity, $\dot{q}$ is heat generation rate per unit volume, and the initial condition and boundary condition are:

$$T(x, y, z, 0) = T_0(x, y, z) \tag{2}$$

and,

$$(-k\nabla T) \cdot \hat{n} = h(T - T_{amb}) \tag{3}$$

where T_0 denotes the initial temperature, T is the temperature at the surface of the powder bed, T_{amb} is the ambient temperature, $\hat{n}$ is the unit outward normal vector, and h is the combined radiative and convective heat transfer coefficient that can be expressed as:

$$h = h_{conv} + \varepsilon\sigma(T^2 + T_{amb}^2)(T + T_{amb}) \tag{4}$$

where h_{conv} defines the convection heat transfer coefficient, σ is the Stefan Boltzmann constant and ϵ is the emissivity of the powder bed, and follows the expression [16]:

$$\varepsilon = f_v\varepsilon_v + (1 - f_v)\varepsilon_s \tag{5}$$

where f_v is the area fraction of the surface that is occupied by the radiation emitting voids, ϵ_s is the emissivity of the solid particle, and ϵ_v is the emissivity of the gaseous void. For a powder bed composed of randomly packed, single-sized spheres [16]:

$$f_v = \frac{0.908\varphi^2}{1.908\varphi^2 - 2\varphi + 1} \tag{6}$$

and,

$$\varepsilon_v = \frac{\varepsilon_s\left[2 + 3.082\left(\frac{1-\varphi}{\varphi}\right)^2\right]}{\varepsilon_s\left[1 + 3.082\left(\frac{1-\varphi}{\varphi}\right)^2\right] + 1} \tag{7}$$

where φ is the fractional porosity of the powder bed and is assumed to be equal to the initial porosity, φ_0, before LMS processing.

In the TEM_{00} mode, the beam emitted from a laser begins as a perfect plane wave with a Gaussian transverse irradiance profile. Patil and Yadava [17] treated the incoming heat flux as internal heat generation in the powder layer by assuming that the energy is evenly distributed with powder thickness. Zhou et al. [18] built a volumetric heat source to investigate single layer laser sintering process, considering that the laser energy obeys the Gaussian law on the surface and decays linearly with sintered depth. For this work, the laser energy density follows a Gaussian profile on the x and y coordinates, and an exponential decay profile on the z coordinate. When laser beam scans along the positive x-direction with a constant velocity v for a period time t, the thermal heat flux follows by definition as:

$$q(x, y, z, t) = \frac{2AP}{\pi R^2\delta} exp\left[-2\frac{(x - vt)^2 + y^2}{R^2}\right] exp\left[-\frac{|z|}{\delta}\right] \tag{8}$$

where A denotes the heat absorptivity of laser beam on the nickel powder bed, P is the laser power, R is the radius corresponding to the point where the laser irradiation diminishes to $1/e^2$ of its maximum value, and δ is the optical penetration depth of the powder bed to the incident laser.

3 Material properties

During laser metal powder material processing, the initial powder properties and distinct phase transition determine to a great extent the thermal field of the sintered sample. Therefore, accurate representation and description of the material properties are essential to properly reflect these characteristics in a numerical model. For this work, the utilized powder was pure nickel powder and the Fe-304 stainless steel was used as the substrate material.

3.1 Thermal conductivity

The conductivities of powder bed and dense solid material differ greatly as adjacent particles only make solid contact over small areas. It follows that the convection and radiation heat transfer mechanism of the fluid inside voids exist in addition to heat conduction. The most popular equation for effective conductivity of the powder bed, k_e, was proposed by Yagi and Kunii [19], for gas-filled voids:

$$\frac{k_e}{k_f} = \frac{\beta(1 - \varphi)}{\gamma\left(\frac{k_f}{k_s}\right) + \frac{1}{\frac{1}{\xi} + \frac{D_p h_{rs}}{k_f}}} + \varphi\beta\frac{D_p h_{rv}}{k_f} \tag{9}$$

where k_f is the thermal conductivity of the fluid surrounding the powder particles, k_s represents the thermal conductivity of the solid, φ is the fractional porosity, D_p is the average diameter of the powder particles, β is the ratio of effective length between the centers to D_p, γ is the ratio of effective length of solid about thermal conduction to D_p, ξ is the ratio of effective thickness of fluid film adjacent to contact surface of two solid particles to D_p which can be empirically taken as $0.02 \times 10^{2(\varphi - 0.3)}$ [20], h_{rs} and h_{rv} are

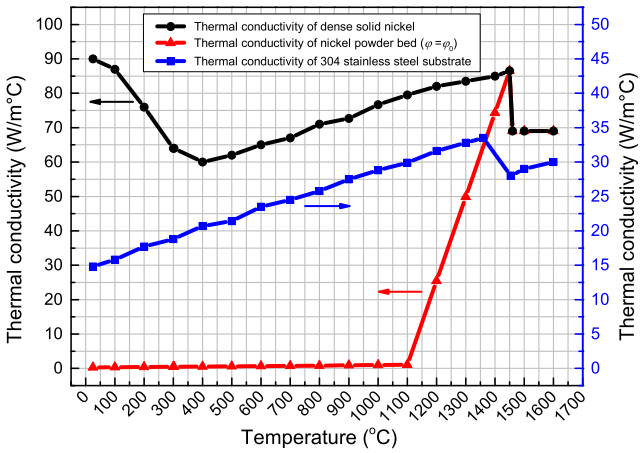

Fig. 1 Thermal conductivity of pure nickel (dense phase and powder phase) and Fe-304 stainless steel as a function of temperature [22]

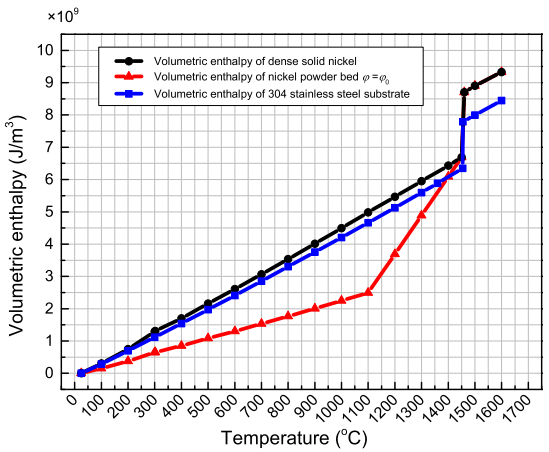

Fig. 2 Volumetric enthalpy of pure nickel (dense phase and powder phase) and Fe-304 stainless steel as a function of temperature [22]

the heat transfer coefficient for radiation from solid to solid and void to void, respectively and are described by [19]:

$$h_{rs} = 0.1952\left(\frac{\varepsilon_s}{2-\varepsilon_s}\right)\left(\frac{T+273.15}{100}\right)^3 \tag{10}$$

and,

$$h_{rv} = \frac{0.1952}{1+\frac{\varphi}{2(1-\varphi)}\cdot\frac{1-\varepsilon_s}{\varepsilon_s}}\left(\frac{T+273.15}{100}\right)^3 \tag{11}$$

where ϵ_s is the emissivity of solid as previously defined. In most case for practical purposes, the values of both β and γ can be assumed as approximately unity. What is more, the thermal conductivity of air embedded inside the voids of the powder bed can be expressed as [21]:

$$k_f = (0.0000586 + 0.00000017639T) \times 418.4 \tag{12}$$

In comparison to the conduction problem of solid material, the thermal conductivity of sintered sample varies from the powder state to the dense state depending on the porosity and temperature of the powder bed. At the initial stage, each element of the powder bed is assumed to be initially powder state, and the thermal conductivity of the powder bed is mainly determined by the porosity, particle diameter, emissivity, and temperature according to Eqs. 9–12. As shown in Fig. 1, during the laser heating stage, once the temperature is higher than the melting point, the powder-to-dense transition will take effect and then the powder elements convert to the dense molten element irreversibly. Therefore, during the cooling stage, the thermal conductivity of the dense phase is only treated as a function of temperature since the liquid phase and solid phase are fully dense.

3.2 Volumetric enthalpy

The enthalpy formulation is used to describe heat transfer in material with phase transitions problems. In this paper, the enthalpy consists two noticeable changes for the sintered material, which are represented by the powder phase to dense phase transition and the mutual transitions between the solid phase and liquid phase.

For the phase transition from powder phase to the dense phase, the volumetric powder enthalpy H_p is related to the enthalpy of dense material H_s as [23]:

$$H_p = \rho_r H_s = (1-\varphi)H_s \tag{13}$$

where ρ_r is the relative density and φ is as previously defined.

For the phase transition from the solid phase to the liquid phase, or vice versa, namely the melt generation and resolidification occur, the latent heat due to melting or fusion is involved, and the energy amount is very considerable that influences the heat transfer dynamics. Dai and Shaw [5] ignored this heat quantity in their research, while Patil and Yadava [17] used a modified specific heat capacity to simulate the heat changes during phase transition. Latent heat should be taken into consideration for the phase transition problem during the LMS process. To account for the latent heat, the volumetric enthalpy of the material is defined as a function of temperature [24]:

$$H(T) = \int_{T_0}^{T} \rho C_p dT, \qquad T < T_s$$
$$H(T) = \int_{T_0}^{T_s} \rho C_p dT + \rho L_m + \int_{T_l}^{T} \rho C_p dT, \quad T > T_l \tag{14}$$

For $T_s \le T \le T_l$, there exists a region in which the melting is partial, and the enthalpy function defined by:

$$H(T) = \int_{T_0}^{T_s} \rho C_p dT + \rho L_m\left(\frac{T-T_s}{T_l-T_s}\right) \tag{15}$$

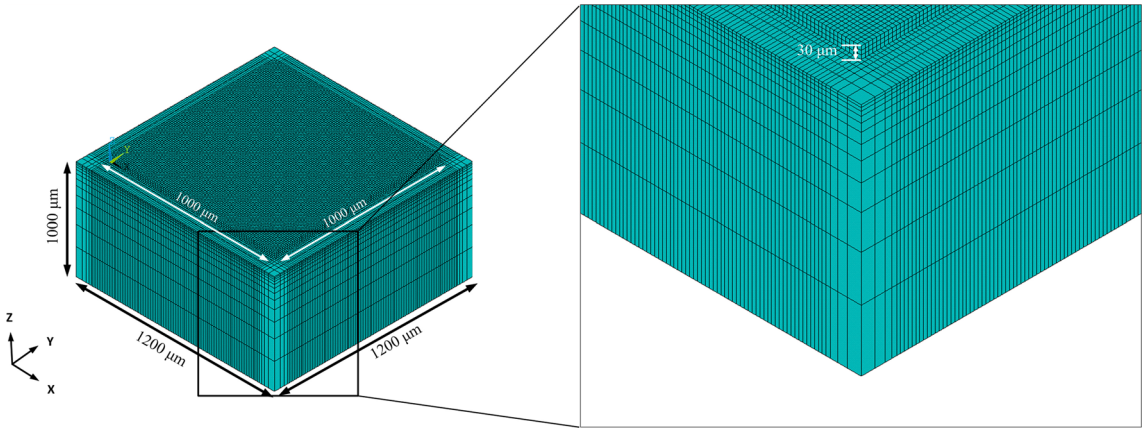

Fig. 3 The entire model and extracted model of the finite element model for numerical simulation

where T_s is the solidus temperature, T_l is the liquidus temperature, L_m is the latent heat of the fusion, T_m is the melting temperature, and T_0 is the reference temperature. Volumetric enthalpy has units of energy/volume and values are derived by integrating specific heat for constant pressure and density between the reference temperature (e.g., 25 °C for this work) and target temperature. Figure 2 shows the temperature-dependent volumetric enthalpy of the dense solid nickel, nickel powder with porosity of φ_0, and Fe-304 stainless steel, respectively. Above the melting point and up to the boiling point, the enthalpy change is assumed to vary linearly maintaining the consistent trend above the melting point.

3.3 Absorptance

The absorptance of a material is a function of number of variables such as wavelength of laser, temperature, phase transitions, surface roughness, packing structure, level of oxidation, etc. For an opaque dense material such as a metal, the absorptance A is defined as [25]:

$$A = \frac{4n}{(n+1)^2 + \kappa^2} \tag{16}$$

where n represents the refractive index and κ is the extinction coefficient. For nickel, the values of n and κ to 1.06 µm radiation are 2.62 and 5.26, respectively [25]. Thus, the absorptance for dense nickel material to 1.06 µm radiation is 0.257, and will be used in this work for the dense phase. While for the nickel powder, it has been extensively known that the use of powder significantly improves the material absorptance of laser energy. For instance, the absorptance of 0.64 of the nickel powder was measured with Nd:YAG laser by Tolochko et al. [12]. Moreover, they found that the particle size had very little influence on the absorptance values and will, therefore, be used for the powder phase in this work.

Table 1 Computational parameters used for finite element analysis

Parameters	Notion	Value
Laser power (W)	P	180
Laser spot radius (µm)	R	50
Scan speed (mm/s)	v	120−900
Initial powder porosity	φ_0	0.5
Average particle size (µm)	D_p	25
Powder bed thickness (µm)	d	30
Optical penetration depth in powder (µm)	δ	30
Absorptance for powder nickel	A_p	0.64
Absorptance for dense nickel	A_s	0.257
Emissivity of dense nickel	ϵ_s	0.33
Ambient temperature (°C)	T_{amb}	25
Initial temperature (°C)	T_0	25
Convection heat transfer coefficient (W/m^2°C)	h_{conv}	25

4 Finite element model description

This analysis was carried out on a three-dimensional meshed geometry model which is a representation of the physical mapping of the sintered sample and substrate. The dimensions of the powder bed are 30 µm in height and 1000 µm in both length and width, while the substrate has a width and length of 1200 µm and height of 1000 µm. In order to apply the convection and radiation boundary conditions, it is indispensable to generate the surface effect element from the basic element as skin wrapping the body. Therefore, the finite element model was built up using two types of elements including thermal 8-node brick elements SOLID70 with a single temperature degree of freedom at each node and SURF152 defined by four nodes from the basic element and an extra node away from the base element.

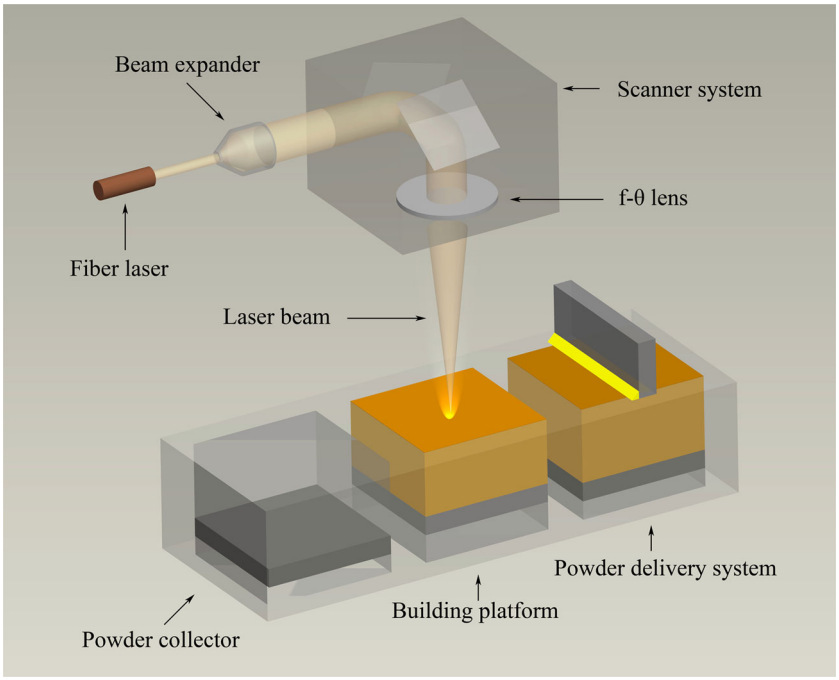

Fig. 4 Schematic diagram of experimental setup for LMS process

In finite element models, the accuracy of the computed results is dictated by the element size and the time increment used in simulations. For model discretization, the scanning length is taken as a whole number multiple of the laser beam diameter, while the element size is set to the whole number divisions of the laser beam area. Moreover, in contrast to the modeling SLS processing, the element size of the powder bed should be much smaller and was taken as 10 µm in our model. The µMKS (termed as µm, kg, s) system of units was employed for the micro-scale modeling and turns out to be efficient [26]. Taking account of the computational precision as well as the elapsed time cost of iterations, the finite element meshes with 175,200 hexahedral elements and about 190,776 nodes have been used for this simulation, which is shown in Fig. 3. In the scanning process of a track, the movement heat source was considered to occur in discrete time steps, and each time period is dictated by the element size and laser flight speed; moreover, the laser beam moves stepwise by one element in the x-direction. The stepping sequence begins at the starting spot and continues until the designated number of tracks is reached. Table 1 summarizes the parameters used in the finite element model.

In order to determine the dimensions of the volumetric heat source, the radius and depth of the laser powder interaction zone are assumed to be equal to the laser beam radius

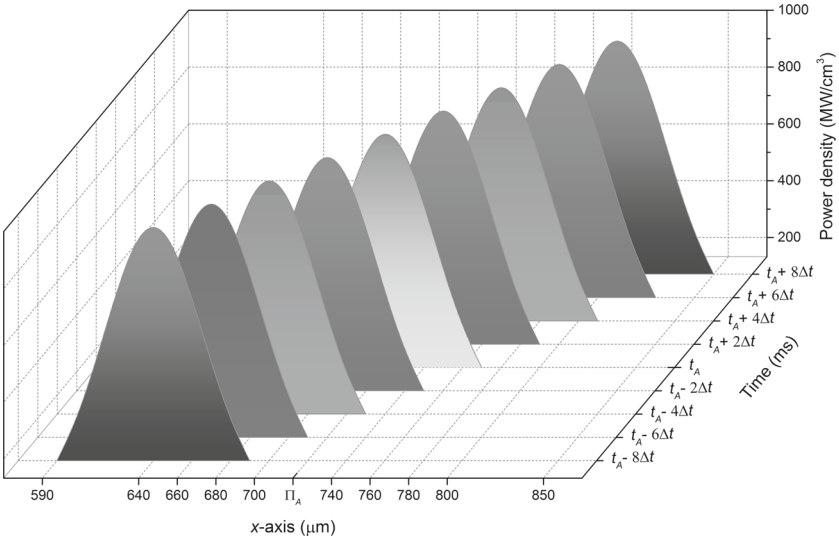

Fig. 5 Schematic of laser scanning over π_A: x=720 µm along x-axis (laser power = 180 W, scan speed = 180 mm/s, laser beam diameter = 100 µm, t_A = 3.14 ms, Δt = 55.56 µs, Δx = 10 µm)

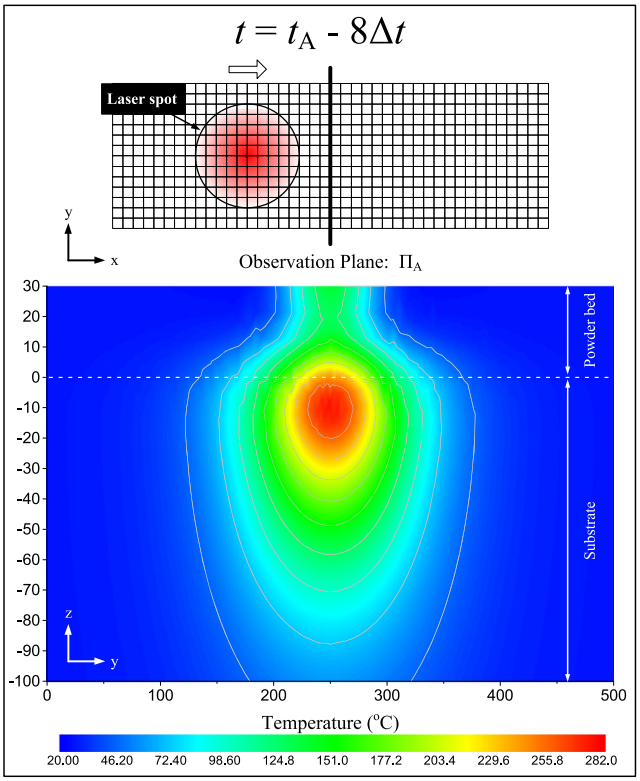

Fig. 6 Temperature contour plot of specified cross-section π_A at time $t = t_A$ - 8Δt=2.70 ms

and the optical penetration depth, respectively. In addition, according to the granulometric properties and layer thickness for the used nickel powder listed in the Table 1 as well as the experimental measurements of optical penetration depth reported in previous study [15], the optical penetration depth is postulated to be equal to the thickness of the powder layer in this work. Moreover, in representing the physical mapping of the laser heat input, the heat source is calculated according to the Gaussian distribution and is applied on the powder bed on which the laser is impinged using table type array parameters [27]. Acherjee et al. [28] established a volumetric Gaussian heat source model using 3D array (x, y, z) parameters as heat source boundary conditions which is developed from their previous study that using 2D array (x, y) parameters to simulate the surface heat flux source [29]. Consequently, it should be noted that it is very significant to take reasonable heat input profile into consideration, and hence the higher dimension table type array parameters appropriate for the volumetric Gaussian heat source should be added into the finite element model. In our study, the volumetric heat generation was created in the form of 4D table type array parameters which contain both the space and time parameters according to the Eq. 8, and is a function of x, y, z coordinates and *time*.

5 Experimental set-up

LMS was performed by a self-developed laser processing system which mainly consisted the continuous wave IPG YLR-200 fiber laser (λ = 1.064 μm, maximum output power of 200 W), an automatic powder delivery system, a building platform, and a computer system for process control. The process parameters with laser power of 180 W, scanning speed of 120–900 mm/s and beam spot size of 100 μm were utilized in the experiment. During LMS, the contents of oxygen and H_2O were both controlled below 20 ppm in an inertia environment. The schematic of LMS process is illustrated in Fig. 4. The metallic powder used in this experiment was the pure nickel powder with a particle size below 38 μm and a mean particle size about 25 μm. For this research, an averaged 30 μm slice thickness of nickel powder was deposited on the Fe-304 stainless steel substrate.

6 Results and discussion

6.1 Thermal field characteristics

The laser beam movement during the LMS processing for over a period of time is shown schematically in Fig. 5. The observation time ranges from $t_A - 8\Delta t$ to $t_A + 8\Delta t$ with

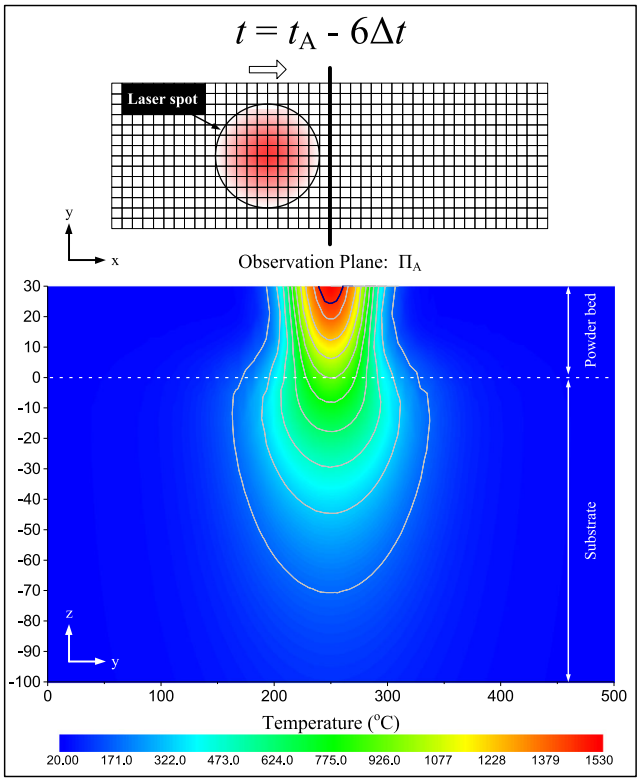

Fig. 7 Temperature contour plot of specified cross-section π_A at time $t = t_A$ - 6Δt=2.81 ms

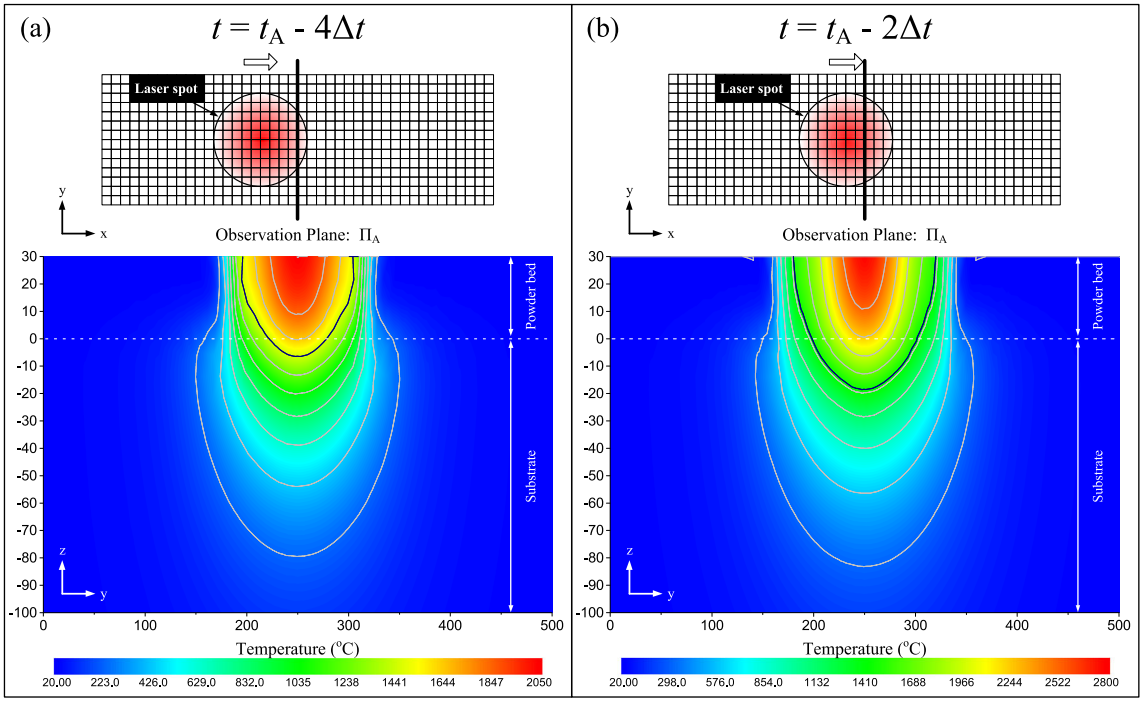

Fig. 8 Temperature contour plot of specified cross section π_A at time **a** $t = t_A - 4\Delta t$=2.92 ms and **b** $t = t_A - 2\Delta t$=3.03 ms

time increment of $2\Delta t$ while the laser power and scan speed are held as constant. t_A is the immediate time step when laser spot center just irradiates π_A after scanning half of the vector length about 0.52 mm, and Δt is the time step for which the laser spot is retained on an element, and can be defined as the element length Δx divided by laser scanning speed v.

This simulation of the impinging laser beam onto the powder bed results in the generation of a molten pool on it. Since the melting point of the nickel and liquidus temperature of Fe-304 stainless steel are almost the same [22], the thick lines (1455 °C) shown both in the powder bed and substrate depict the dimensions of the molten pool, and it can be measured through temperature distribution of the sintered part while laser moves along scanning path. The width of the molten pool is taken from the molten material along the y-direction perpendicular to the laser scanning direction, while the melted depth is measured from the top surface of the powder bed to the molten depth along the z-direction as obtained on the cross section of the y-z plane.

As predicted by the finite element model, Figs. 6, 7, 8, 9, 10, and 11 demonstrate the contour plot series of temperature and molten pool evolution of the specified cross section obtained at each time step. Figure 6 shows the contour plot of cross-section π_A at time $t = t_A - 8\Delta t$=2.70 ms. It can be seen that, different to the other plots, the maximum temperature (T_{max} = 281.43 °C) lies in the area of substrate (z<0) near the powder/substrate interface instead of the powder bed layer (z>0). At this time, for the laser radius R of 50 μm, the distance between beam spot center and the cross-section location D_A is 80 μm, which indicates that the plane π_A is a non-irradiated region. It can be deduced that the heat flux obtained by π_A is all from the previous laser irradiated region at this time. Moreover, because the thermal conductivity of substrate material Fe-304 stainless steel (∼18.8 W/m °C at 300 °C) is much higher than that of the nickel powder (∼0.46 W/m °C at 300 °C), the heat flux from laser-irradiated region in the substrate area of π_A is higher than that in the powder layer area, therefore, the average temperature of the substrate area is larger than that of the powder layer area. In other words, the substrate heated by the fore laser-irradiated region has preheating effect on rear powder bed region during the laser scanning.

Figure 7 shows the temperature contour plot of plane π_A at time $t = t_A - 6\Delta t$ = 2.81 ms. The simulation results reveal that although the plane π_A is still a non-irradiated region at this moment, the sharply increased maximum temperature T_{max} lies in the top surface of the powder layer (z=30 μm). The maximum temperature of 1526.70 °C exceeds the melting point and exists a little amount of liquid formation. Moreover, because the energy distribution obeys volumetric Gaussian distribution on the surface and decays exponentially with depth, the peak heat flux is at the top surface and melts the nickel powder around the laser spot. As a result, the nickel powder elements located between beam spot and the plane π_A change to dense elements immediately. It is noted that the thermal conductivity of dense molten nickel (∼69 W/m °C) is more than two times that of the substrate

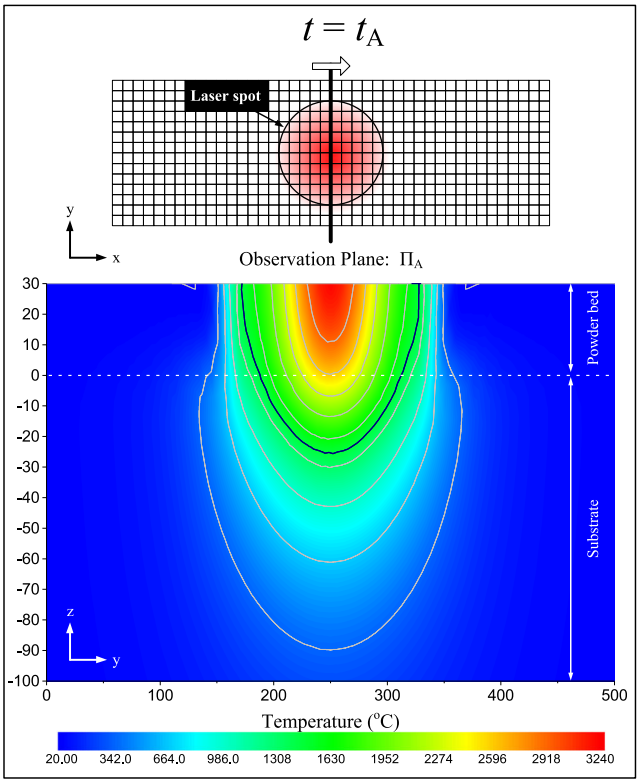

Fig. 9 Temperature contour plot of specified cross-section π_A at time $t = t_A = 3.14$ ms

material, the heat flux from laser-irradiated region in the powder layer area of π_A is higher than that in the substrate area. Consequently, as laser approaching closer to plane π_A, because of the combined effects of the transition of powder-to-dense and the difference of thermal conductivity between the powder and the substrate material, the mechanism of preheating the nickel powder changes for the heat source from 304 stainless steel substrate to molten nickel in the previous laser-irradiated region.

Figure 8a, b are the temperature contour plots of plane π_A at time $t = t_A - 4\Delta t = 2.92$ ms and $t = t_A - 2\Delta t = 3.03$ ms, respectively. The centers of the laser beam spot are 680 and 700 µm along x-axis, which indicate that the cross-section locates within the laser spot region already. Therefore, in comparison with Fig. 7, the maximum temperature increases steeply to 2048.81 and 2793.29 °C, respectively. Moreover, the molten pool width and depth at $t = 2.92$ ms are 115.04 and 36.48 µm, whereas at $t = 3.03$ ms are 141.16 and 48.63 µm, respectively. It should be noted that molten pool depths are larger than the powder bed thickness (30 µm). This observation implies that the substrate region of plane π_A begins to melt and the molten dimensions will increase with the laser spot exposure time.

The temperature contour plots for time steps when the laser beam is scanning over plane π_A are presented in Figs. 9 and 10a, b. The maximum temperature T_{max} of π_A attains its peak value (~3234.34 °C) at $t_A = 3.14$ ms when the center of laser spot is just at π_A, then T_{max} is observed to decrease by 145.01 °C at $t_A + 2\Delta t = 3.25$ ms and by 645.5 °C at $t_A + 4\Delta t = 3.36$ ms. Different from the decreasing trend of the maximum temperature after laser spot crossing over

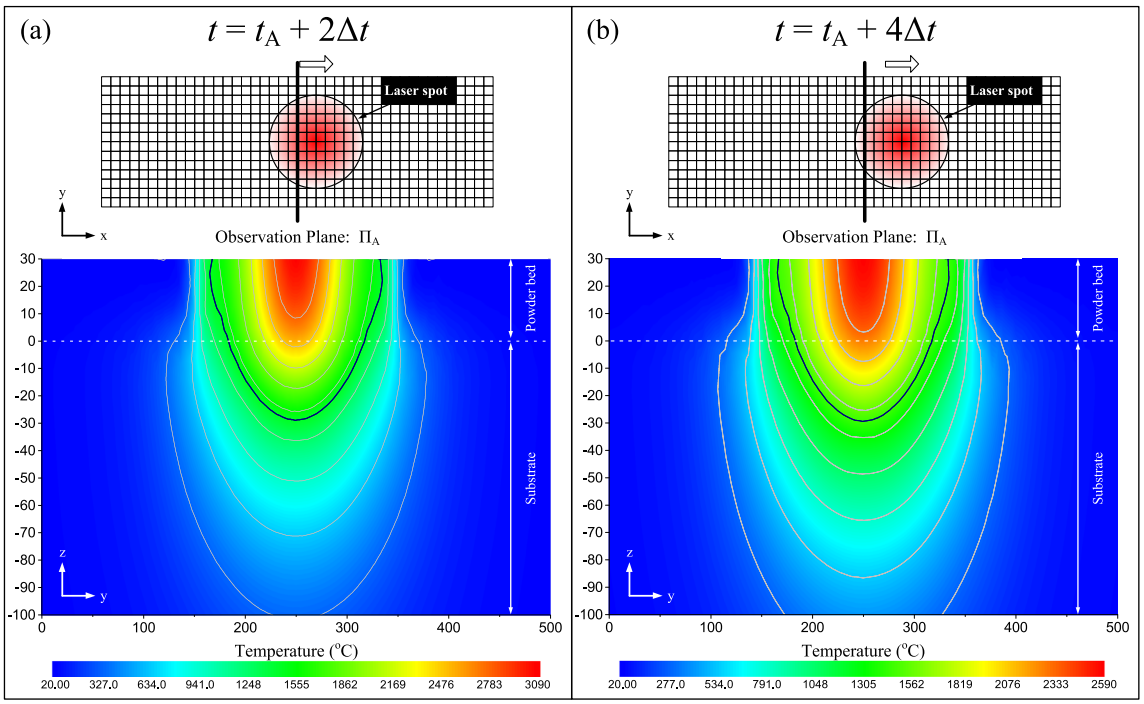

Fig. 10 Temperature contour plot of specified cross section π_A at time **a** $t = t_A + 2\Delta t = 3.25$ ms and **b** $t = t_A + 4\Delta t = 3.36$ ms

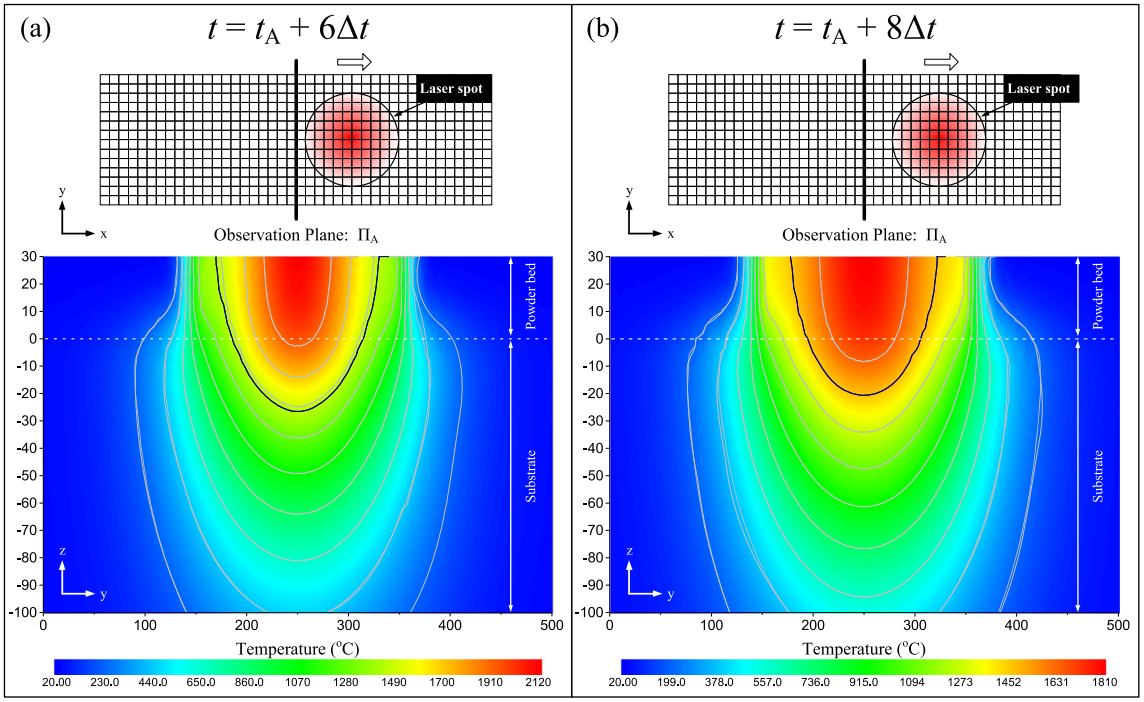

Fig. 11 Temperature contour plot of specified cross section π_A at time **a** $t = t_A + 6\Delta t = 3.48$ ms and **b** $t = t_A + 8\Delta t = 3.59$ ms

plane π_A, the molten pool width reaches its peak value of ~175 μm at $t_A + 2\Delta t = 3.25$ ms, which appears $2\Delta t$ earlier than the time step when the molten pool depth reaches its peak value (~59.46 μm at $t_A + 4\Delta t = 3.36$ ms). This results from the fact that the volumetric heat source follows an exponential depth profile on the z-direction. Furthermore, also from these figures, it can be seen that the evolution of molten pool dimensions is a little delay than the evolution of maximum temperature. Therefore, it can be inferred that the molten pool is asymmetric pertaining to the center of the laser spot area. The results further demonstrate that the center of the molten pool slice is slightly shifted toward the reverse direction of laser scanning and the deviation is estimated to be about $2\Delta t \times v$=20 μm ~ $4\Delta t \times v$=40 μm under current laser processing conditions. This phenomenon can be ascribed to the thermal accumulation effect that the rear laser-irradiated region has the post heating influence on the previously solidified area (e.g., π_A) which is now in a molten state with steeply increased thermal conductivity.

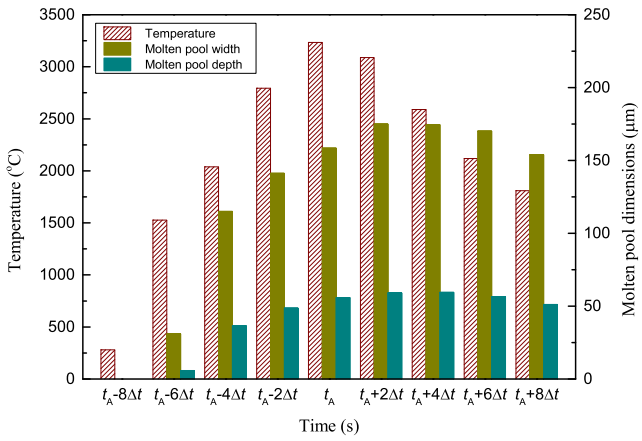

Fig. 12 The maximum temperature, molten pool width and molten pool depth of plane π_A versus time during the laser scanning

The thermal accumulation effect can also explain the phenomenon that from the intermediate time step of Fig. 11a ($t = t_A + 6\Delta t = 3.48$ ms) to the intermediate time step of Fig. 11b ($t = t_A + 8\Delta t = 3.59$ ms). The maximum temperature of the powder bed at 3.48 and 3.59 ms are 2118.76 and 1809.36 °C. Moreover, the molten pool width and depth at 3.48 ms are 170.17 and 56.64 μm, and at 3.59 ms are 154.0 and 51.14 μm, respectively. It can be found that for the time step of the laser beam moves away from plane π_A (e.g., $t = t_A + 8\Delta t = 3.58$ ms), although the maximum temperature has decreased sharply by 44 % in π_A, the molten pool width and depth have decreased slightly by 12 and 14 %, respectively. Furthermore, it can be inferred that the molten pool depth has a higher cooling rate compared to the molten pool width. This phenomenon can be attributed to the fact that as the laser scans along the x-axis of the powder bed, the elements adjacent to the y-direction of the molten pool region are still in powder state, while the elements adjacent to the z-direction of the molten pool are dense substrate elements, the substrate material with higher thermal conductivity allows more heat transfer from the molten pool in a short period of time. Therefore, when the laser moves away

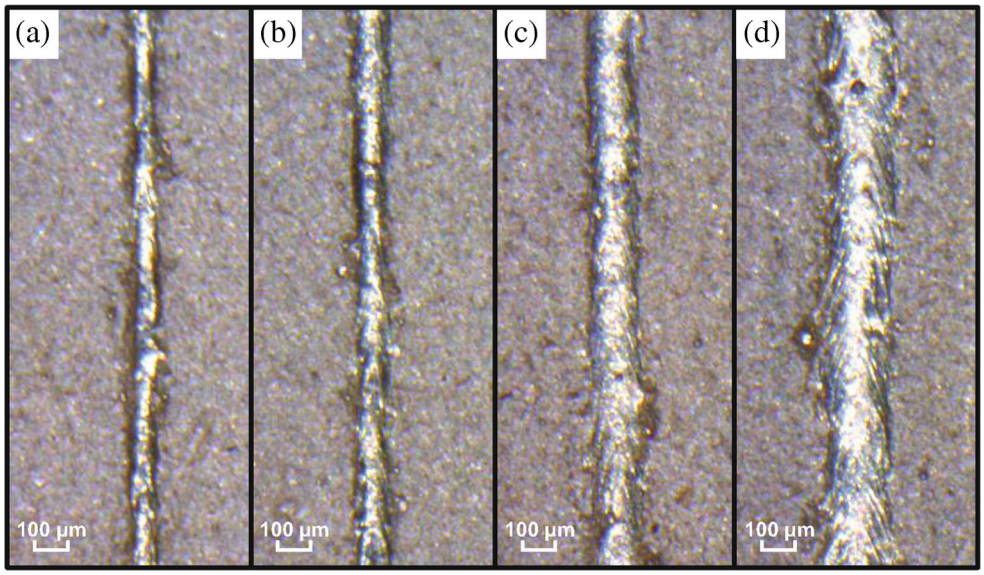

Fig. 13 Single scan track profiles under different line energy: **a** 200 J, **b** 300 J, **c** 600 J, and **d** 1000 J

from the cross-section, the maximum temperature gradient along z-direction (∼13.97 °C/μm) during the fabrication process at $t = t_A + 8\Delta t = 3.58$ ms is lower than that along the y-direction (∼54.79 °C/μm).

The variation of the molten pool width and depth versus time is given in Fig. 12. It is found that the heating and cooling rate regarding plane π_A are 1.09×10^7 °C/s and 5.87×10^6 °C/s, respectively. The molten pool width and depth increase sharply as the laser approaches while decrease slowly when the laser moves away. The maximum molten pool depth of 59 μm melts not only the current layer height but also deeper into the substrate region resulting in adequate condition for metallurgical bonding between the sintered layer and the substrate.

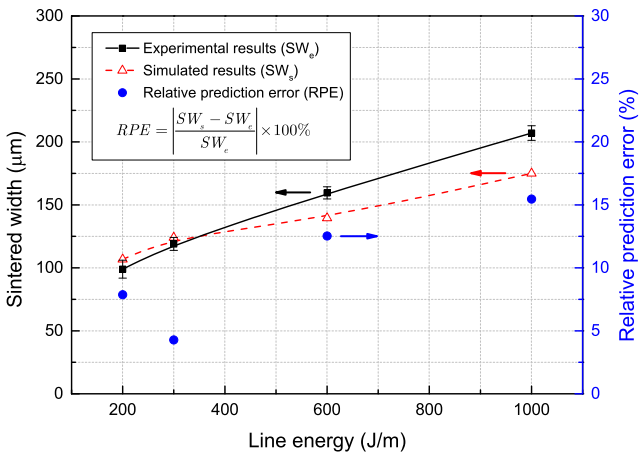

Fig. 14 Comparison of experimental and simulated results as function of line energy (SW_e experimental sintered width, SW_s simulated sintered width)

6.2 Experimental verification

In order to verify the model, the simulated widths are compared to the experimental sintered results as function of line energy and the other processing parameters are held as constants. The experimental sintered widths were observed and measured by an optical microscopy (Nikon Epiphot 300). Figure 13 shows single scan track profiles under different line energy. As shown in Fig. 14, the simulated and experimental results increased with the line energy due to the larger molten pool dimensions produced by the more energy input. For the lower line energy, it is evident that the predicted sintered widths are in good accordance with the experimental measurements. The relative prediction errors (RPE) of sintered widths are below 16 % for line energy from 200 to 1000 J/m which is also in the process window. It should be noted that for the higher line energy (>300 J/m), the predicted sintered widths are smaller than that of experimental results and the difference between them increases with the line energy. This discrepancy in higher line energy can be ascribed to the facts that the more amount of liquid generated from higher heat input results in a larger molten pool dimensions which will cause partial melting around the sintered tracks and thus increases the sintered width. The similar experimental results were reported by [30]; they studied the movement of powder materials using a microscope setup, and found that powders moved toward the melting pool because of surface tension during laser sintering process. Furthermore, note that the maximum temperature shown in the contour plot (see Fig. 9) will exceed the boiling point of nickel (2730 °C), and the boiling and vaporization may lead to a recoil which has a flattening effect on the molten pool dimensions. However, despite the differences discussed above, the results show

good agreement between the predicted and the measured values.

7 Conclusions

In order to understand the physical mechanism of LMS processing, the energy absorption and penetration is indispensable for a more reliable finite element model, therefore, the realistic material state transition and laser heat input profile should be taken into account. In this paper, a three-dimensional finite element model that encompasses the utilization of powder-to-dense transition sub-model involving effective thermal conductivity, volumetric enthalpy, and absorptance change in combination with a sub-model of a moving volumetric Gaussian heat source to determine temperature distribution and molten pool dimensions in LMS of nickel powder on 304 stainless steel substrate has been established. Based on these computational investigations, the following conclusions can be drawn.

The previous laser-irradiated region has pre-heating effect on rear non-irradiated region. As the laser approaches to a specified cross section, the maximum temperature moves from substrate region near the powder/substrate interface to the top surface of powder bed; furthermore, the mechanism of preheating the nickel powder changes for the heat source from 304 stainless steel substrate to molten nickel in the previous laser-irradiated region.

The rear laser-irradiated region has post-heating effect on the fore laser-irradiated region. As the laser moves away from a cross section, the decrease ratio of molten pool dimensions is gentler than that of maximum temperature, the molten pool depth has a higher cooling rate than the molten pool width. Moreover, the center of the molten pool slice is slightly shifted toward the reverse direction of laser scanning due to the thermal accumulation effect and the deviation is also estimated under current laser processing conditions.

The simulated results showed a reasonable agreement with experimental measurements. The simulated and experimental results as well as the differences between them increase with the line energy. Moreover, relative prediction errors of sintered widths are below 16 % within the process window.

Acknowledgements This work is supported by the National Natural Science Foundation of China (61475056, 51429501), the Natural Science Foundation of Hubei Province of China (2014CFA049), and the Fundamental Research Funds for the Central Universities, HUST: 2013QT002. The authors would also thank Prof. Zemin Wang and Dr. Kai Guan for their immense experimental suggestion and assistance.

References

1. Regenfuss P, Hartwig L, Klotzer S, Ebert R, Brabant T, Petsch T, Exner H (2005) Industrial freeform generation of microtools by laser micro sintering. Rapid Prototyping J 11(1):18–25. doi:10.1108/13552540510573356
2. Regenfuss P, Streek A, Hartwig L, Klotzer S, Brabant T, Horn M, Ebert R, Exner H (2007) Principles of laser micro sintering. Rapid Prototyping J 13(4):204–212. doi:10.1108/13552540710776151
3. Zhu H, Ke L, Lei W, Dai C, Chen B (2013) Effect of the Q-switch parameters on the sintering behavior of laser micro sintering Cu-based metal powder using Q-switched Nd:YAG laser. Rapid Prototyping J 19(1):44–50. doi:10.1108/13552541311292727
4. Ke L, Zhu H, Yin J, Wang X (2014) Effect of peak laser power on laser micro sintering of nickel powder by pulsed Nd:YAG laser. Rapid Prototyping J 20(4):328–335. doi:10.1108/RPJ-09-2012-0084
5. Dai K, Shaw L (2004) Thermal and mechanical finite element modeling of laser forming from metal and ceramic powders. Acta Mater 52(1):69–80. doi:10.1016/j.actamat.2003.08.028
6. Kolossov S, Boillat E, Glardon R, Fischer P, Locher M, 2004 3D FE simulation for temperature evolution in the selective laser sintering process. Int J Mach Tools Manuf 44(2–3):117–123. doi:10.1016/j.ijmachtools.2003.10.019
7. Roberts IA, Wang CJ, Esterlein R, Stanford M, Mynors DJ (2009) A three-dimensional finite element analysis of the temperature field during laser melting of metal powders in additive layer manufacturing. Int J Mach Tools Manuf 49(12–13):916–923. doi:10.1016/j.ijmachtools.2009.07.004
8. Dong L, Makradi A, Ahzi S, Remond Y (2009) Three-dimensional transient finite element analysis of the selective laser sintering process. J Mater Process Technol 209(2):700–706. doi:10.1016/j.jmatprotec.2008.02.040
9. Hussein A, Hao L, Yan C, Everson R (2013) Finite element simulation of the temperature and stress fields in single layers built without-support in selective laser melting. Mater Des 52:638–647. doi:10.1016/j.matdes.2013.05.070
10. Sun SB, Zheng LJ, Liu YY, Liu JH, Zhang H (2015) Selective laser melting of Al-Fe-V-Si heat-resistant aluminum alloy powder: modeling and experiments. Int J Adv Manuf Technol:1–11. doi:10.1007/s00170-015-7137-8
11. Kizaki Y, Azuma H, Yamazaki S, Sugimoto H, Takagi S (1993) Phenomenological studies in laser cladding. Part I. Time-resolved measurements of the absorptivity of metal powder. Jpn J Appl Phys 32(part 1):205–212
12. Tolochko NK, Laoui T, Khlopkov YV, Mozzharov SE, Titov VI, Ignatiev MB (2000) Absorptance of powder materials suitable for laser sintering. Rapid Prototyping J 6(3):155–160. doi:10.1108/13552540010337029
13. Taylor CM (2004) Direct laser sintering of stainless steel: thermal experiments and numerical modelling, Ph.D. The University of Leeds Leeds
14. Wang XC, Laoui T, Bonse J, Kruth JP, Lauwers B, Froyen L (2002) Direct selective laser sintering of hard metal powders: experimental study and simulation. Int J Adv Manuf Technol 19(5):351–357. doi:10.1007/s001700200024
15. Fischer P, Romano V, Weber HP, Karapatis NP, Boillat E, Glardon R (2003) Sintering of commercially pure titanium powder with a Nd:YAG laser source. Acta Mater 51(6):1651–1662. doi:10.1016/s1359-6454(02)00567-0
16. Sih SS, Barlow JW (1995) Emissivity of powder beds. In: Marcus H, Beaman J, Barlow J, Bourell D, Crawford R (eds) Proceedings of the 6th Annual SFF Symposium, Austin. The University of Texas, pp 402–408

17. Patil RB, Yadava V (2007) Finite element analysis of temperature distribution in single metallic powder layer during metal laser sintering. Int J Mach Tools Manuf 47(7–8):1069–1080. doi:10.1016/j.ijmachtools.2006.09.025
18. Zhou W, Wang X, Hu J, Zhu X (2013) Melting process and mechanics on laser sintering of single layer polyamide 6 powder. Int J Adv Manuf Technol:1–8. doi:10.1007/s00170-013-5113-8
19. Yagi S, Kunii D (1957) Studies on effective thermal conductivities in packed beds. AIChE Journal 3(3):373–381. doi:10.1002/aic.690030317
20. Xue S, Barlow J (1991) Models for the prediction of the thermal conductivities of powders. In: Marcus H, Beaman J, Barlow J, Bourell D, Crawford R (eds) Proceedings of the 2nd Annual SFF Symposium, Austin, The University of Texas, pp 62–69
21. Sih SS, Barlow JW (1994) Measurement and prediction of the thermal conductivity of powders at high temperatures. In: Marcus H, Beaman J, Barlow J, Bourell D, Crawford R (eds) Proceedings of the 5th Annual SFF Symposium, Austin, The University of Texas, pp 321–329
22. Mills KC (2002) Recommended values of thermophysical properties for selected commercial alloys. Woodhead Publishing, Cambridge
23. Tolochko NK, Arshinov MK, Gusarov AV, Titov VI, Laoui T, Froyen L (2003) Mechanisms of selective laser sintering and heat transfer in Ti powder. Rapid Prototyping J 9(5):314–326. doi:10.1108/13552540310502211
24. Kamara AM, Marimuthu S, Li L (2014) Finite element modeling of microstructure in laser-deposited multiple layer Inconel 718 parts. Mater Manuf Process 29(10):1245–1252. doi:10.1080/10426914.2014.930963
25. Steen WM, Mazumder J (2010) Laser material processing. Springer, New York
26. Yin J, Zhu H, Ke L, Lei W, Dai C, Zuo D (2012) Simulation of temperature distribution in single metallic powder layer for laser micro-sintering. Comput Mater Sci 53(1):333–339. doi:10.1016/j.commatsci.2011.09.012
27. ANSYS (2005) APDL Programmer's Guide. SAS IP Inc, Canonsburg PA 15317
28. Acherjee B, Kuar AS, Mitra S, Misra D (2012) Effect of carbon black on temperature field and weld profile during laser transmission welding of polymers: a FEM study. Opt Laser Technol 44(3):514–521. doi:10.1016/j.optlastec.2011.08.008
29. Acherjee B, Kuar AS, Mitra S, Misra D (2010) Finite element simulation of laser transmission welding of dissimilar materials between polyvinylidene fluoride and titanium. Int J Eng Sci Technol 2(4):176–186
30. Fan K, Cheung W, Gibson I (2001) Material movement and fusion behavior of TrueForm and TrueForm/SiO2 during selective laser sintering. In: Bourell D (ed) Proceedings of the 12th Annual SFF Symposium, Austin. The University of Texas, pp 146–154